applied optics

# Coded aperture design in mismatched compressive spectral imaging

LAURA GALVIS,[1] HENRY ARGUELLO,[2,*] AND GONZALO R. ARCE[1]

[1]Department of Electrical and Computer Engineering, University of Delaware, Newark, Delaware 19716, USA
[2]Department of Computer Science, Universidad Industrial de Santander, Bucaramanga 680002, Colombia
*Corresponding author: henarfu@uis.edu.co

Received 10 August 2015; revised 21 October 2015; accepted 22 October 2015; posted 22 October 2015 (Doc. ID 247570); published 17 November 2015

**Compressive spectral imaging (CSI) senses a scene by using two-dimensional coded projections such that the number of measurements is far less than that used in spectral scanning-type instruments. An architecture that efficiently implements CSI is the coded aperture snapshot spectral imager (CASSI). A physical limitation of the CASSI is the system resolution, which is determined by the lowest resolution element used in the detector and the coded aperture. Although the final resolution of the system is usually given by the detector, in the CASSI, for instance, the use of a low resolution coded aperture implemented using a digital micromirror device (DMD), which induces the grouping of pixels in superpixels in the detector, is decisive to the final resolution. The mismatch occurs by the differences in the pitch size of the DMD mirrors and focal plane array (FPA) pixels. A traditional solution to this mismatch consists of grouping several pixels in square features, which subutilizes the DMD and the detector resolution and, therefore, reduces the spatial and spectral resolution of the reconstructed spectral images. This paper presents a model for CASSI which admits the mismatch and permits exploiting the maximum resolution of the coding element and the FPA sensor. A super-resolution algorithm and a synthetic coded aperture are developed in order to solve the mismatch. The mathematical models are verified using a real implementation of CASSI. The results of the experiments show a significant gain in spatial and spectral imaging quality over the traditional grouping pixel technique.** 

***OCIS codes:*** (110.0110) Imaging systems; (110.4234) Multispectral and hyperspectral imaging.

http://dx.doi.org/10.1364/AO.54.009875

## 1. INTRODUCTION

Spectral imaging systems acquire large amounts of data by sequentially scanning either the spatial or spectral coordinates. The resulting signals are merged to construct a spectral data cube or three-dimensional (3D) data set, known as a spatiospectral data cube. Push-broom spectral imaging sensors, for instance, measure the spectrum at each spatial point in the scene through a slit spectrometer. In these sensors, there is a spatial motion of the slit or the object in order to acquire the whole data cube [1]. A limitation of these sensing techniques is that the number of zones to scan grows linearly in proportion to the desired spatial and spectral resolution. In contrast, compressive spectral imaging (CSI) systems sense the 3D data cube through just a few two-dimensional (2D) measurements of the coded and spectrally dispersed source field. These systems have gained popularity since they require fewer measurements than those attained with traditional hyperspectral imaging sensors [2–4].

A CSI architecture that efficiently attains coded measurements is the coded aperture snapshot spectral imager (CASSI). It captures 2D coded aperture projections of the spatiospectral data cube by using a coded aperture and a dispersive element. An inverse problem is solved to reconstruct the spectral images by using a linear program or a greedy pursuit on a basis where the undersampled signals admit sparse representations.

The coded apertures in CASSI are often implemented through photomasks attached to piezoelectric devices [5]. An improvement on this configuration has been proposed in order to facilitate the capture of multiple projections or snapshots, each admitting a different coded aperture pattern [5–7]. The replacement of the photomask by digital micromirror devices (DMDs) allows multicoding, or the capture of multiple shots, at video rates without the displacement of the optical elements on the system. Further, the DMD transmission efficiency is comparable to that offered by the photomask. Despite the selection of the coding element, the resolution has to be considered. Usually, the resolution or number of pixels of the DMD is different than that exhibited by the detector. The mismatch of the DMD mirrors and the detector pixels is such that pixel-to-pixel correspondence is not achieved. This issue also occurs in detectors at $\gamma$- and $x$-ray wavelengths [8]. The traditional

approach to match the resolution of the CASSI elements consists in grouping several pixels in square features. The maximum resolution of the system is then given by the element with lower resolution, subutilizing the resolution of the other element [9].

More formally, let $N_1 \times N_1$ be the resolution of the coded aperture and $N_2 \times N_2$ the resolution of the focal plane array (FPA). Two possible cases of mismatching can take place, which are analyzed by defining the relation between the resolutions of the detector and the coded aperture as $N_1/p_1 = N_2/p_2$, where $p_1$ and $p_2$ are integers. The first case occurs when $P = \frac{p_1}{p_2} > 1$, which means that $N_1 > N_2$, and the second case occurs when $P' = \frac{p_2}{p_1} > 1$, meaning that $N_1 < N_2$. To alleviate this mismatch, several pixels can be grouped such that the resulting spatial resolution of the CASSI system is determined by $\min\{N_1, N_2\}$, which subutilizes the DMD or FPA resolutions. This paper develops two methods to fully utilize the maximum resolution of the coded aperture and the detector. The first case, $P > 1$, follows the same rationale as super-resolution approaches, where the idea is to translate high-resolution scenes into low-resolution detectors. A super-resolution technique is applied in this case to exploit the high resolution of the coded aperture in the CASSI system. In the second case, $P' > 1$, the design of a synthetic coded aperture that allows full utilization of the detector resolution is proposed.

The main contribution of this paper is the development of a mathematical model for the CASSI with pixel pitch mismatch between the coded aperture and the detector. Two cases of mismatch are analyzed and modeled, allowing the reconstruction of a high-resolution spatiospectral data cube. The mathematical models developed are verified by using a real implementation of CASSI. Finally, the real reconstructions demonstrate the improvement obtained by using this approach instead of the traditional grouping of pixels.

## 2. CASSI MODEL WITH PIXEL GROUPING

The CASSI architecture is composed of a coded aperture, a dispersive element, and an FPA as illustrated in Fig. 1. It captures multiplexed (2D) projections of a spatiospectral data cube using a snapshot. The spatiospectral power source density is defined as $f_0(x, y, \lambda)$, where $(x, y)$ index the spatial dimensions and $\lambda$ indexes the wavelength. The source is first coded by a coded aperture $T(x, y)$ where the black pixels block the impinging light and the white pixels permit light to pass through, resulting in the coded field $f_1(x, y, \lambda)$. The resulting coded field is then spectrally dispersed by a dispersive element. The impulse response of this component is $h(x' - S(\lambda) - x, y' - y)$, where

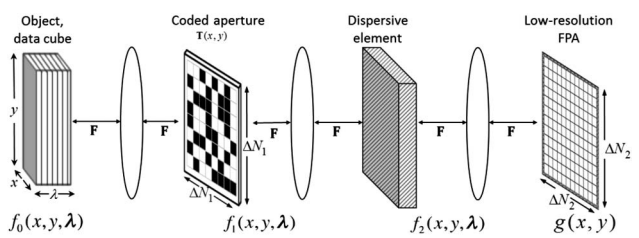


**Fig. 1.** CASSI architecture is illustrated. The data cube is coded, spectrally dispersed, and integrated on the FPA.

$S(\lambda) = \alpha(\lambda)(\lambda - \lambda_c)$ accounts for the dispersion induced by the prism along the $x$ axis and $\lambda_c$ is the central wavelength, which is not dispersed by the prism.

Before the integration on the detector, the output can be expressed as

$$f_2(x, y, \lambda) = \iint T(x', y') f_0(x', y', \lambda) \times h(x' - S(\lambda) - x, y' - y)\mathrm{d}x'\mathrm{d}y'. \quad (1)$$

The compressive measurement at the focal plane array results from the integration of the coded and dispersed data fields $f_2(x, y, \lambda)$ over the detector's spectral range sensitivity ($\Lambda$). The compressive measurement is represented as $g(x, y) = \int_\Lambda f_2(x, y, \lambda)\mathrm{d}\lambda$.

When several FPA measurements are captured with each one using a different coded aperture $T^\ell(x, y)$, the energy in front of the 2D FPA can be expressed as

$$g^\ell(x, y) = \int_\Lambda T^\ell(x - S(\lambda), y) f_0(x - S(\lambda), y, \lambda)\mathrm{d}\lambda, \quad (2)$$

for $\ell = 0, 1, \ldots, K - 1$, where $K$ is the number of snapshots. The discretized compressive measurement at the respective pixel of the detector is given by

$$g^\ell_{mn} = \iint p(m, n; x, y) g^\ell(x, y)\mathrm{d}x\mathrm{d}y, \quad (3)$$

where $p(m, n; x, y) = \mathrm{rect}(\frac{x}{\Delta_d} - m, \frac{y}{\Delta_d} - n)$ accounts for the detector pixelation in the detector, $\Delta_d = D_2/N_2$ is the pitch of the detector pixels, and $D_2$ is the size of the detector. Replacing Eq. (2) in Eq. (3) leads to

$$g^\ell_{mn} = \iiint \mathrm{rect}\left(\frac{x}{\Delta_d} - m, \frac{y}{\Delta_d} - n\right) \times T^\ell(x - S(\lambda), y) f_0(x - S(\lambda), y, \lambda)\mathrm{d}x\mathrm{d}y\mathrm{d}\lambda. \quad (4)$$

The transmittance function of the coded aperture is given by

$$T^\ell(x, y) = \sum_{m', n'} t^\ell_{m'n'} \mathrm{rect}\left(\frac{x}{\Delta_c} - m', \frac{y}{\Delta_c} - n'\right), \quad (5)$$

where $\Delta_c = D_1/N_1$ is the pitch of the coded aperture, $D_1$ is the size of the coded aperture, and $t^\ell_{m'n'}$ is the discretized version of the coded aperture $T^\ell(x, y)$.

Traditionally, the optical system can be designed such that $D_1 = D_2 = D$. This can be established through the prescription of the lens in the system to obtain an adequate magnification [3]. When $N_1 \neq N_2$, such that there is a pixel pitch mismatch $\Delta_c = D_1/N_1 \neq \Delta_d = D_2/N_2$, it is usual to artificially match the DMD and FPA resolutions. A common strategy consists of grouping several pixels in square features. This grouping reduces the resolution of the system, which is given by $N = \min\{N_1, N_2\}$. This strategy implicates a significant reduction of the spatial and spectral resolution of the measurements and therefore of the reconstructions [10,11].

When the pixels are grouped into square features such that $N = N_1/p_1 = N_2/p_2$, the integration of the continuous field $g(x, y)$ in a single $(m, n)^{\mathrm{th}}$ detector pixel in Eq. (4) can be expressed as

$$g^{\ell}_{mn} = \sum_{m',n'} t^{\ell}_{m'n'} \iiint \mathrm{rect}\left(\frac{x - S(\lambda)}{\Delta} - m', \frac{y}{\Delta} - n'\right) \times \mathrm{rect}\left(\frac{x}{\Delta} - m, \frac{y}{\Delta} - n\right) f_0(x - S(\lambda), y, \lambda)\mathrm{d}x\mathrm{d}y\mathrm{d}\lambda, \quad (6)$$

where $\Delta = D/N$. Equation (6) is the forward model of CASSI, which has been recently extended to account for the nonlinearity of the dispersive element [6]. In this new model, the energy from a single voxel is mapped onto three detector pixels, such that each source voxel can be split into three regions, $R_0$, $R_1$, and $R_2$. Figure 2 illustrates a zoomed version of the regions of the source voxel affecting one pixel on the detector. The corresponding energy of each region that impinges in the $(m, n)^{\mathrm{th}}$ detector pixel is represented by the weights $w_{mnku}$, where $m$, $n$ index the spatial coordinates, $k$ is the spectral dimension, and $u$ accounts for the regions $R_0$, $R_1$, and $R_2$ of the source voxel. More specifically, $w_{mnku} = (\iiint_{R_u} \mathrm{d}x\mathrm{d}y\mathrm{d}\lambda)(\iiint_{R_1 \cup R_2 \cup R_3} \mathrm{d}x\mathrm{d}y\mathrm{d}\lambda)^{-1}$. The following discrete notation is used to reformulate the FPA measurement. The source $f_0(x, y, \lambda)$ can be written as $F_{mnk}$, where $m$ and $n$ index the spatial coordinates and $k$ determines the $k$th spectral band. The discretized coded aperture is $t^{\ell}_{m'n'}$ as indicated in Eq. (5). Using this notation, the FPA measurement in Eq. (6) can be written as

$$g^{\ell}_{mn} = \sum_{k=0}^{L-1} \sum_{u=0}^{2} w_{mnku} t^{\ell}_{m(n-k-u)} F_{m(n-k-u)k}, \quad (7)$$

where $m, n = 0, 1, \ldots, N - 1$, $k = 0, 1, \ldots, L - 1$, $u = 0, 1, 2$, and $\ell = 0, 1, \ldots, K - 1$. The number of resolvable bands $L$ is determined by the detector resolution $\Delta$. The spatial resolution $N$ is determined for both the FPA and coded aperture resolutions.

The analysis of the physical sensing phenomena in the CASSI system when $N_1 \neq N_2$ allows us to develop different strategies to overcome the mismatch. Figure 3 illustrates an example of a mismatch, where more than one row of detector pixels receives the coded and dispersed light; in this particular case, it occurs given the high resolution of the detector.

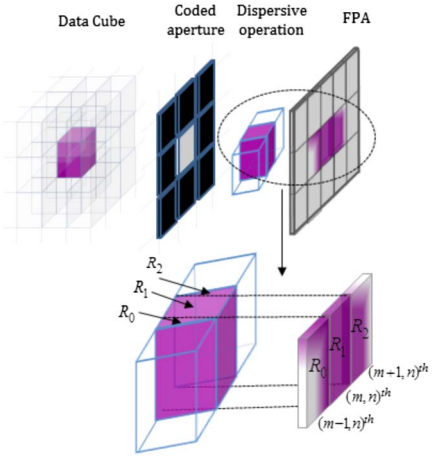


**Fig. 2.** Spatiospectral data flow in the CASSI architecture. The source is coded by the coded aperture and dispersed by a prism. A source voxel is zoomed to identify the regions $R_0$, $R_1$, and $R_2$.

## 3. CASSI WITH PIXEL MISMATCH

The CASSI with pixel mismatch is developed with the aim to solve the mismatching problem when $N_1 > N_2$ and $N_1 < N_2$. In the first case, a super-resolution model is proposed to exploit the high coded aperture resolution. For the latter, the approach corresponds to the creation of a synthetic coded aperture in order to reconstruct the spectral images at the high detector resolution.

### A. Mismatching by Super-Resolution

This case of mismatching occurs when the coded aperture resolution is higher than the FPA resolution. The approach to overcome this mismatching is to apply super-resolution to the model in Eq. (7). This is possible if the detector element pitch is greater than the Nyquist sample-limited resolution given by the wavelength of the light imaged [12,13]. The energy impinging on one detector pixel is divided by the number of coded aperture pixels that match that detector pixel. This subpixel division is included in the model in Eq. (7). The number of subpixels in a detector pixel $P$ or the super-resolution factor, respectively, in the $x$ and $y$ dimensions depends on the number of coded aperture pixels matching one detector pixel following $N = N_1 = PN_2$. A decimation of the $(m, n)^{\mathrm{th}}$ detector pixel is defined as

$$g^{\ell}_{mn} = \sum_{q=0}^{P-1} \sum_{r=0}^{P-1} \hat{g}^{\ell}_{iP-q,jP-r}, \quad (8)$$

where $\hat{g}^{\ell}_{ij}$ is the measurement at the subpixel level and $i, j = 0, 1, \ldots, N_2(P - 1)$. In addition, the dispersion effect must be modeled at the subpixel level in the horizontal dimension in both the coded aperture and the source. Equation (7) is then rewritten including the subpixel decimation and the dispersion effect as

$$g^{\ell}_{mn} = \sum_{q=0}^{P-1} \sum_{r=0}^{P-1} \sum_{k=0}^{L-1} \sum_{u=0}^{2} w_{(mP-q)(nP-r)ku} \times t^{\ell}_{((mP-q-k)-k-u)(nP-r)} F_{((mP-q-k)-k-u)(nP-r)k}, \quad (9)$$

where $F \in \mathbb{R}^{N^2 L}$, $t^{\ell} \in \mathbb{R}^{N^2}$, and $g \in \mathbb{R}^{N/P(N/P+L/P-1)}$. Notice the lower resolution of the detector compared with the coded aperture.

The forward model in Eq. (9) allows use of the full coded aperture resolution instead of the resolution exhibited by the detector, and as a result it is possible to obtain a high spatial resolution reconstruction. Figure 4 (left) shows a traditional approach example, where $2 \times 2$ pixels are grouped at the coded aperture to match the resolutions. The super-resolution CASSI (SR-CASSI) in Fig. 4 (right) instead takes advantage of the full resolution of the coded aperture and proposes a solution with $P = 2$ to emulate a detector with the resolution of the coded aperture.

### B. Mismatching by Synthetic Coded Apertures

The opposite case occurs when the FPA resolution is higher than that of the coded aperture. Since a pixel in the coded aperture is mapped into several pixels on the detector, the proportion of the coded aperture pixels as they are projected onto the detector pixels defines a synthetic gray-scale, higher resolution coded aperture. Thus, the projections attained by the system could be realized by a coded aperture matching the detector pixel size, with the exception that the coded aperture values

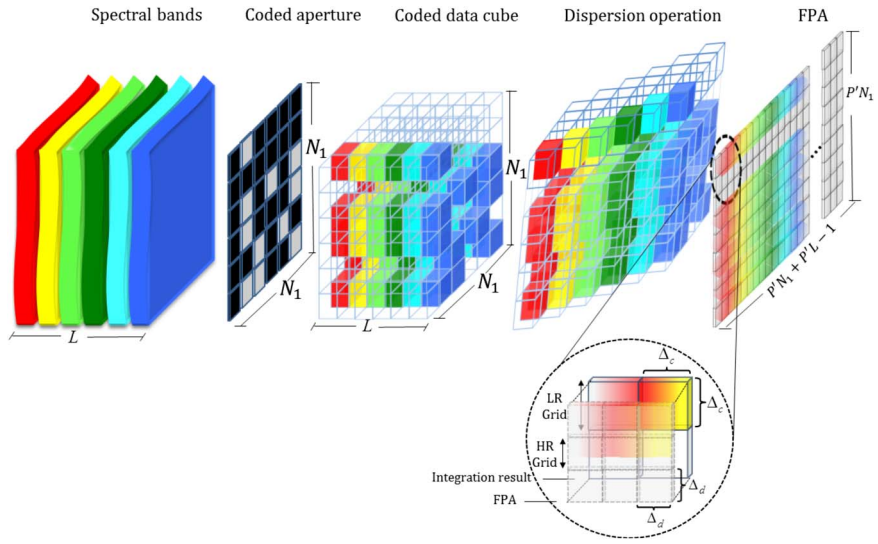


**Fig. 3.** Physical sensing phenomena in CASSI; $L$ spectral bands of the data cube $F$ are coded spatially by a coded aperture $t$ and dispersed by the prism. The detector captures the intensity $g$ by integrating the coded light. The pixel pitch mismatch is depicted and zoomed; the FPA detector receives the coded and dispersed light, but it is missing a pixel-to-pixel correspondence. The high resolution of the detector is therefore subutilized.

needed to realize the projection are in this case gray-scale, which models the proportion that is mapped from the coded aperture pixel into each of the detector pixels. It should be noted that a higher resolution gray-scale code is not used in the projection. It is only a model used to describe the physical phenomena of the pixel mismatch and is then used into the reconstruction of the data cube. The FPA resolution replaces $\Delta$ in Eq. (6) using $N = P'N_1 = N_2$. The resulting $g^{\ell}_{mn}$ measurement includes the intensity of the corresponding $P'^2$ detector pixels. Traditionally, the measurement fails to exploit the subpixel information; the Synthetic-CASSI seeks to reach the level of resolution of the subpixels. More specifically, Eq. (6) should be reformulated as

$$g^{(1)\ell}_{mn} + g^{(2)\ell}_{mn} + \ldots + g^{(P'^2)\ell}_{mn} = \sum_{m',n'} t^{\ell}_{m'n'} \iiint \mathrm{rect}\left(\frac{x - S(\lambda)}{P'\Delta_c} - m', \frac{y}{P'\Delta_c} - n'\right) \times \mathrm{rect}\left(\frac{x}{P'\Delta_c} - m, \frac{y}{P'\Delta_c} - n\right) f_0(x - S(\lambda), y, \lambda)\mathrm{d}x\mathrm{d}y\mathrm{d}\lambda. \quad (10)$$

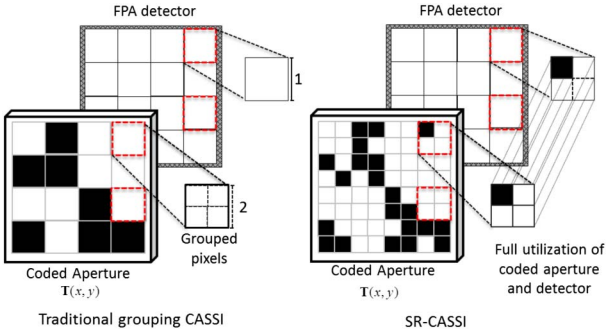


**Fig. 4.** (Left) Grouping of pixels at the coded aperture in traditional CASSI. (Right) Matching of the coded aperture and detector resolutions in SR-CASSI.

A synthetic coded aperture with higher resolution is defined, in order to take into account the intensity on each $g^{(\mathrm{th})\ell}_{mn}$ of the left side on Eq. (10). Hence, the translation of the coded aperture $t^{\ell}_{m'n'}$ into one with higher resolution directly related with $N_2$ accounts for the mismatching effect produced by the resolution differences on the coded aperture and detector. This matching is done through the creation of a synthetic coded aperture. The synthetic coded aperture defined as $\hat{t}_{m'n'}$ is tuned in, and the FPA measurement at the $N$ resolution is expressed as

$$g^{(i)\ell}_{mn} = \sum_{m'n'} \hat{t}^{\ell}_{m'n'} \iiint \mathrm{rect}\left(\frac{x - S(\lambda)}{\Delta} - m', \frac{y}{\Delta} - n'\right) \times \mathrm{rect}\left(\frac{x}{\Delta} - m, \frac{y}{\Delta} - n\right) f_0(x - S(\lambda), y, \lambda)\mathrm{d}x\mathrm{d}y\mathrm{d}\lambda, \quad (11)$$

where $\Delta = D/N_2$ and $i$ index each of the pixels at the detector. The synthetic coded aperture $\hat{t}_{m'n'}$ in Eq. (11) can be succinctly expressed as

$$\hat{t}_{m'n'} = \alpha(\beta t_{m',n'} + (1-\beta)t_{m',n'+1}) + (1-\alpha)(\beta t_{m'+1,n'} + (1-\beta)t_{m'+1,n'+1}). \quad (12)$$

The synthetic coded aperture is defined in terms of $\alpha$ and $\beta$, accounting for the horizontal and vertical fraction of a pixel at the coded aperture that is reflected in the synthetic pixel of $\hat{t}_{m'n'}$, and the evaluation of the neighbours of the pixel $(i,j)$ in the original discrete version of the coded aperture $t_{m'n'}$. These neighbors are denoted as $t_{m',n'}, t_{m',n'+1}, t_{m'+1,n'}, t_{m'+1,n'+1}$. The $\alpha$ and $\beta$ fractions can be expressed as

$$\alpha = \begin{cases} B, & B > 0 \\ 1, & B = 0 \end{cases}, \qquad \beta = \begin{cases} C, & C > 0 \\ 1, & C = 0 \end{cases}, \quad (13)$$

where $B$ and $C$ are defined in terms of the ratio between the coded aperture and the FPA pixel pitch $P' = \frac{p_2}{p_1}$ as follows:

$$B = \left\lfloor \frac{(n+1)}{P'} \right\rfloor P' - n, \quad (14)$$

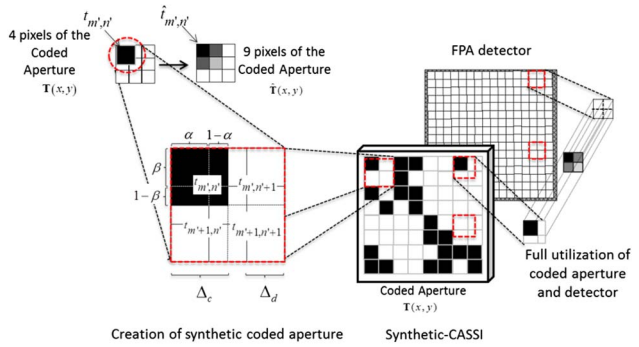


**Fig. 5.** (Left) Translation from a coded aperture into its synthetic version. (Right) Matching of the coded aperture and detector resolutions through the use of a synthetic coded aperture.

$$C = \lfloor \frac{(m+1-k-u)}{P'} \rfloor P' - (m-k-u). \tag{15}$$

Figure 5 (left) shows the translation from a small set of pixels of a coded aperture into its respective synthetic coded aperture. Figure 5 (right) shows the matching of the resolutions through the creation of a synthetic coded aperture to fully utilize the detector resolution. Notice the higher resolution of the synthetic coded aperture and detector in the Synthetic-CASSI.

The discretized Synthetic-CASSI model is then expressed as

$$g^{\ell}_{mn} = \sum_{k=0}^{(L-1)P'} \sum_{u=0}^{2} w_{mnku} \hat{t}^{\ell}_{m(n-k-u)} \mathcal{F}_{m(n-k-u)k}, \tag{16}$$

where the spatial and spectral resolutions of this measurements are dictated by $P'$ such that $m, n = 0, 1, \ldots, (N-1)P'$ and $k = 0, 1, \ldots, (L-1)P'$.

## 4. RECONSTRUCTION ALGORITHM

The hyperspectral signal $\mathbf{F} \in \mathbb{R}^{N \times N \times L}$, or its vector representation $\mathbf{f} \in \mathbb{R}^{N \cdot N \cdot L}$, is $S$-sparse on some basis $\mathbf{\Psi}$, such that $\mathbf{f} = \mathbf{\Psi\theta}$ can be approximated by a linear combination of $S$ vectors from $\mathbf{\Psi}$ with $S \ll (N \cdot N \cdot L)$. Alternatively, the CASSI projections in Eqs. (9) and (16) can be expressed as $\mathbf{g} = \mathbf{H\Psi\theta} = \mathbf{A\theta}$ where $\mathbf{H}$ is a matrix whose structure is determined by the coded aperture entries and the dispersive element effect, and the matrix $\mathbf{A} = \mathbf{H\Psi}$ is the sensing matrix. This algorithm solves the optimization problem

$$\tilde{f} = \mathbf{\Psi}\{\text{argmin}_{\boldsymbol{\theta}} \|\mathbf{g} - \mathbf{H\Psi\theta}\|_2 + \tau\|\boldsymbol{\theta}\|_1\}, \tag{17}$$

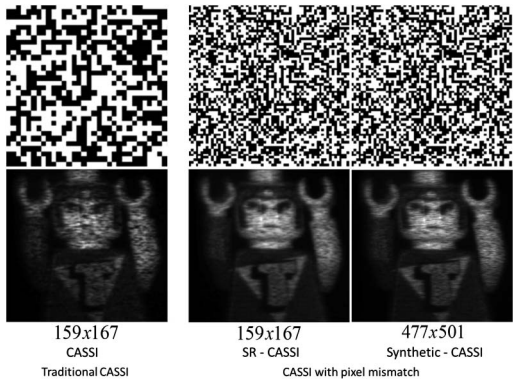


**Fig. 6.** Coded apertures and measurements for (left) traditional CASSI and (right) CASSI with pixel mismatch. The projections attained with the CASSI with pixel mismatch model have a high resolution compared with those obtained with the traditional CASSI.

where $\boldsymbol{\theta}$ is an $S$-sparse representation of $\mathbf{f}$, and $\tau$ is a regularization constant [14]. The basis representation $\mathbf{\Psi}$ is set as the Kronecker product of two bases $\mathbf{\Psi} = \mathbf{\Psi}_1 \otimes \mathbf{\Psi}_2$, where $\mathbf{\Psi}_1$ is a 2D wavelet Symmlet 8 basis and $\mathbf{\Psi}_2$ is the 1D discrete cosine transform.

The compressive sensing gradient projection for sparse reconstruction (GPSR) algorithm is used to obtain the reconstructions of the data cube [15]. The methods proposed in this paper, in essence, increase the resolution of the reconstructed data cubes, and consequently the inverse problem deals with large sets of pixels to be reconstructed. As such, the computational complexity of the reconstruction increases in proportion to the added spatial and spectral resolution. The computational complexity is determined by the particular reconstruction algorithm. In this case, the GPSR complexity is $\mathcal{O}(KN^4L)$ per iteration, where $K$ is the number of snapshots, $N^2$ is the spatial resolution, and $L$ is the number of spectral bands. Hence, the complexity in the two approaches described is determined also by the $P > 1$ and $P' > 1$ factors. The computational complexity is then $\mathcal{O}(KN^4P^4L)$ for the mismatching by super-resolution and $\mathcal{O}(KN^4P'^4L)$ in the case of the mismatching by synthetic coded apertures.

## 5. EXPERIMENTAL RESULTS

The CASSI system was experimentally realized to demonstrate the CASSI with pixel mismatch performance. The coded apertures were implemented in a Texas Instruments D1100 DMD

**Table 1. Comparison of the Traditional CASSI and CASSI with Pixel Mismatch Specifications[a]**

| | | Mirrors and Pixels Pitch Sizes (μm) | | Resolution (Pixels) | | |
|---|---|---|---|---|---|---|
| **Cases** | | $\Delta_c$ | $\Delta_d$ | Coded Aperture | Spatial Recons. | Spectral Recons. |
| **Traditional CASSI** | $159 = 318/2 = 477/3$ | $\Delta_c = 27.36^b$ | $\Delta_d = 29.7^c$ | 159 × 159 | 159 × 159 | 8 |
| **SR-CASSI** | $318 = 318 = (2)159$ | $\Delta_c = 13.68$ | $\Delta_d = 29.7^c$ | 318 × 318 | 318 × 318 | 8 |
| **Synthetic-CASSI** | $477 = (3/2)318 = 477$ | $\Delta_c = 13.68$ | $\Delta_d = 9.9$ | 318 × 318 | 477 × 477 | 24 |

[a]The number of resolvable bands is determined by $\Delta_d$.
[b]2 × 2 grouping of pixels.
[c]3 × 3 grouping of pixels.

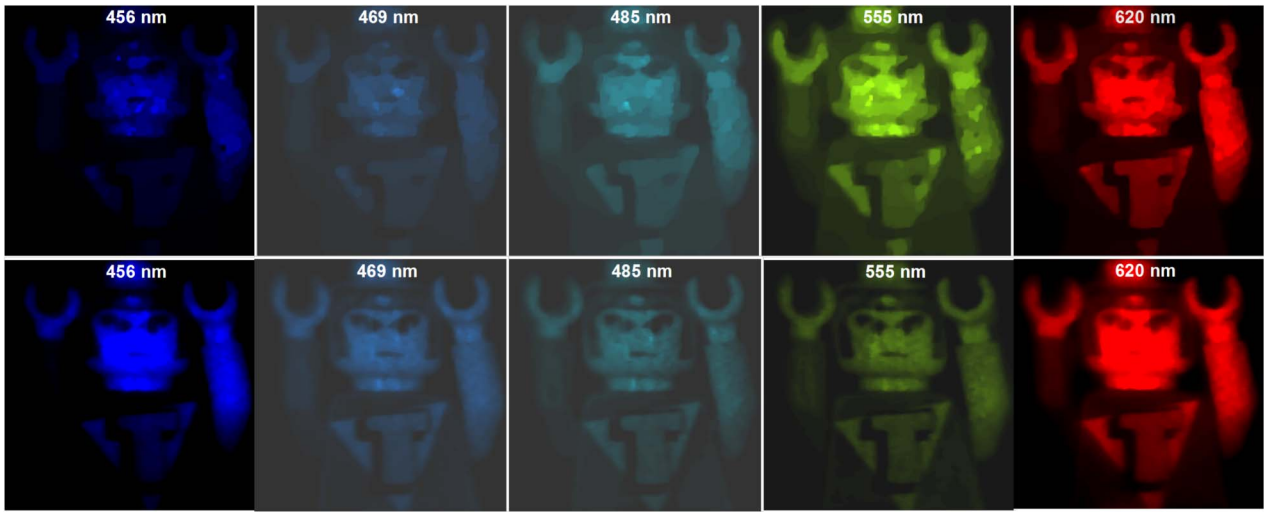


**Fig. 7.** Experimental reconstructions of five spectral bands. (Top) Traditional CASSI, (bottom) SR-CASSI. The improvement in the spatial quality achieved with the SR-CASSI can be easily noticed.

(DLP), a custom double Amici prism (Shangai Optics) was used as a dispersive element, and an FPA detector (Stingray F-033B) captured the measurements. The nonlinear dispersion curve of the prism was determined experimentally by using a monochromator. The DMD used to implement the coded apertures has a resolution of $1024 \times 768$ and a mirror pitch size of $\Delta_c = 13.68$ μm.

The FPA detector used in this experimental setup has a resolution of $656 \times 492$ pixels and a pitch size of $\Delta_d = 9.9$ μm.

Three sets of compressive measurements were acquired by using the CASSI optical setup. The sets correspond to the traditional CASSI, the SR-CASSI and the Synthetic-CASSI measurements, respectively. In the traditional CASSI, the pixels are grouped into square features to match the resolutions on the coded aperture and the detector using the relation $N = N_1/p_1 = N_2/p_2$, where $p_1 = 2$, $p_2 = 3$, $N_1 = 318$, and $N_2 = 477$. In this traditional case, the reconstructed images have a low spatial resolution of $159 \times 159$ pixels due to the grouping process. Also, this grouping approach limits the number of spectral bands to eight. For the three cases a sensing ratio of 50% was used, and the GPSR algorithm was used to recover the spatiospectral data cube [15]. Table 1 shows the specifications of the three set of measurements.

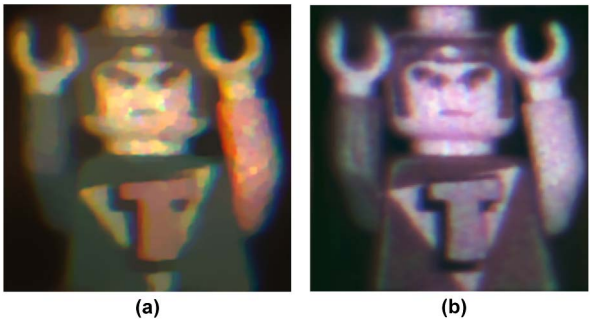


**Fig. 8.** RGB profile of the (a) traditional and (b) SR-CASSI reconstructions. The SR-CASSI achieves a smoothed reconstruction compared with the traditional result.

A visual comparison of the coded apertures and measurements is presented in Fig. 6, top and bottom, respectively. $318 \times 318$ DMD mirrors were used to implement the coded apertures for the three sets. The traditional approach, however, requires the grouping of pixels, which reduces the actual resolution of the coded aperture designed (top left), compared with the high resolution of the coded apertures implemented in the CASSI with pixel mismatch (top right). On the other hand, the traditional CASSI measurements in Fig. 6 (bottom left) have low resolution; the measurements resolution for the first case of mismatching (SR-CASSI) is the same as in the traditional case, but the codification using a high-resolution coded aperture produces a more detailed 2D projection. The Synthetic-CASSI measurements have a high resolution as well as a codification with a high-resolution coded aperture.

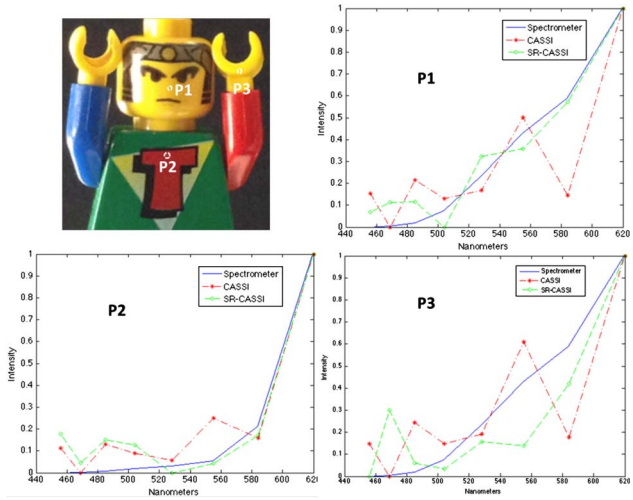


**Fig. 9.** Spectral signatures of three different spatial points. Traditional CASSI and SR-CASSI signatures are compared with the original spectral responses. The spectral curves obtained with the SR-CASSI are closer to the originals.

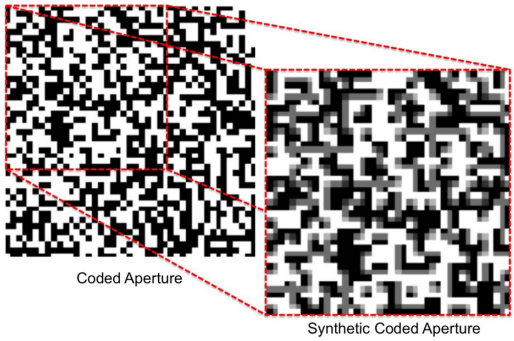


**Fig. 10.** Synthetic coded aperture with the resolution of the detector is created. This synthetic coded aperture is used in the reconstruction process.

### A. SR-CASSI Reconstructions

The measurements for the SR-CASSI were acquired implementing a coded aperture with a resolution of $N_1 = 318$ pixels. To emulate a low-resolution detector, its pixels were grouped into $3 \times 3$ square features representing one low-detector pixel for $N_2 = 159$ such that $P = 2$. After the application of the SR-CASSI model in Eq. (9) and applying the GPSR algorithm that solves the optimization problem in Eq. (17), the measurements and the reconstructions have the coded aperture resolution; this is $318 \times 318$ pixels. Therefore, the coded aperture resolution is fully utilized. In this case, the number of resolvable bands is eight.

The traditional CASSI reconstructions were interpolated to the resolution of the SR-CASSI approach, $318 \times 318 \times 8$, to compare the results. Figure 7 illustrates five spectral bands for the traditional CASSI and the SR-CASSI, respectively. It can be observed that the SR-CASSI results outperforms the results attained with the traditional approach.

Figure 8 shows a RGB profile of the traditional and SR-CASSI. The details in the SR-CASSI reconstruction can be easily noticed. The spectral signatures for three points randomly chosen are shown in Fig. 9. The points are indicated in the original RGB image as P1, P2, and P3. The original signature, obtained using a commercially available spectrometer (Ocean Optics USB2000+), is compared with the traditional CASSI and the SR-CASSI signatures. The curves obtained by using the SR-CASSI are closer to the original.


**Fig. 11.** RGB profile of the (a) traditional and (b) Synthetic-CASSI reconstructions. Synthetic-CASSI yields a smoothed image, retaining the details of the scene.

### B. Synthetic-CASSI Reconstructions

In the third set of measurements, the Synthetic-CASSI is tested using a resolution of $N_1 = 318$ pixels to implement the coded aperture, and as a result, the FPA measurement has a resolution of $N_2 = 477$ pixels such that $P' = 3/2$. Applying the Synthetic-CASSI model in Eq. (16), a synthetic coded aperture with the same used resolution of the detector is created to reconstruct the spatiospectral data cube. Figure 10 shows a coded aperture and its equivalent synthetic coded aperture such as that used to reconstruct the data-cube. Then the final spatial resolution of the reconstructed images is $477 \times 477$ pixels. As a result, the detector resolution is fully utilized. In this case, the high resolution of the FPA permits us to achieve 24 spectral bands.

In order to compare the results, the traditional CASSI reconstructions were interpolated to the resolution of the Synthetic-CASSI approach, $477 \times 477 \times 24$. The RGB profiles

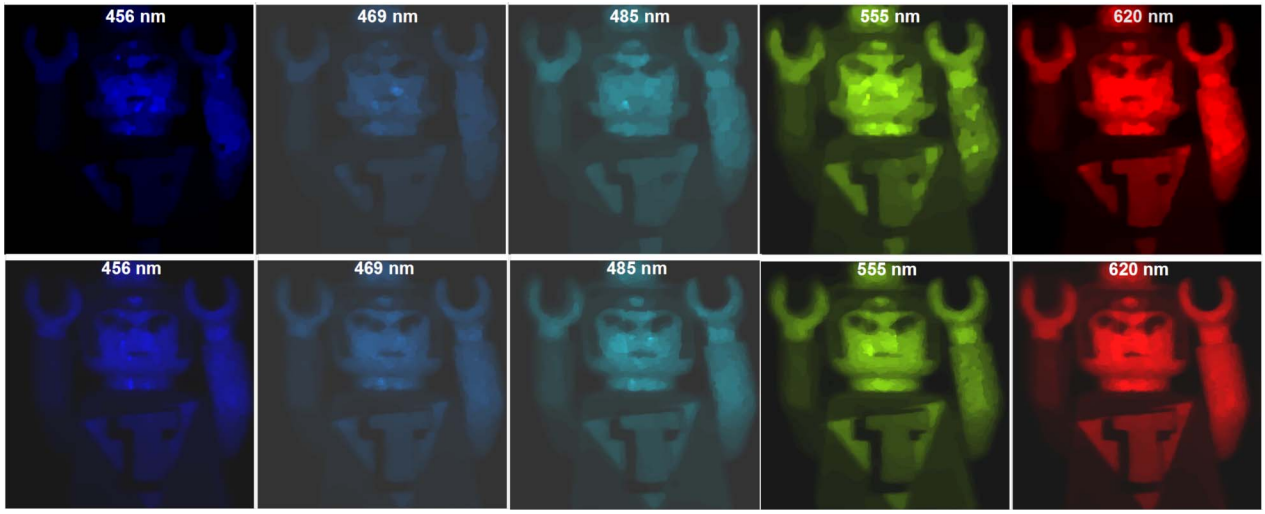


**Fig. 12.** Experimental reconstructions of five spectral bands. (Top) Traditional CASSI, (bottom) Synthetic-CASSI. It can be seen that Synthetic-CASSI results outperform the results achieved by the traditional CASSI.

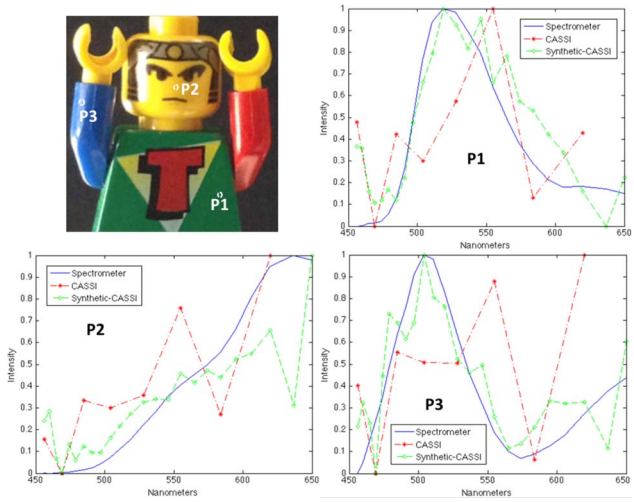


**Fig. 13.** Spectral signatures of three different spatial points. Traditional CASSI and Synthetic-CASSI signatures are compared with the original spectral responses. The improved results can be noticed in the spectral signatures achieved by the Synthetic-CASSI.

of the traditional and Synthetic-CASSI are depicted in Fig. 11. The improvement in the spatial quality can be easily noticed. Figure 12 shows five spectral bands for the traditional CASSI and the Synthetic-CASSI. The improvement in the spatial quality can be observed.

The spectral signatures of three randomly selected points are compared with the signatures obtained using a spectrometer in Fig. 13. The points are indicated as P1, P2, and P3. Again, it can be seen how the curves using the Synthetic-CASSI are closer to the originals, which demonstrates the improvement of the model.

## 6. CONCLUSION

A mathematical model for the CASSI with pixel mismatch has been developed. The model exploits the resolution of the DMD and FPA, which determine the resolution of the reconstructions. The model accounts for two different cases of mismatching. In the first case, a super-resolution model is proposed to exploit the coded aperture resolution. In the second case, the creation of a synthetic coded aperture is proposed in order to reconstruct the spectral images at the detector resolution. Real reconstructions show the spatial and spectral improvement achieved with the proposed model in comparison with traditional approaches of grouping pixels.

## REFERENCES

1. R. G. Sellar and G. D. Boreman, "Classification of imaging spectrometers for remote sensing applications," Opt. Eng. **44**, 013602 (2005).
2. G. R. Arce, D. J. Brady, L. Carin, H. Arguello, and D. S. Kittle, "An introduction to compressive coded aperture spectral imaging," IEEE Signal Process. Mag. **31**(1), 105–115 (2014).
3. A. A. Wagadarikar, R. John, R. Willett, and D. Brady, "Single disperser design for coded aperture snapshot spectral imaging," Appl. Opt. **47**, B44–B51 (2008).
4. C. Li, T. Sun, K. Kelly, and Y. Zhang, "A compressive sensing and unmixing scheme for hyperspectral data processing," IEEE Trans. Image Process. **21**, 4002–4015 (2012).
5. D. Kittle, K. Choi, A. A. Wagadarikar, and D. J. Brady, "Multiframe image estimation for coded aperture snapshot spectral imagers," Appl. Opt. **49**, 6824–6833 (2010).
6. H. Arguello, H. Rueda, Y. Wu, D. W. Prather, and G. R. Arce, "Higher-order computational model for coded aperture spectral imaging," Appl. Opt. **52**, D12–D21 (2013).
7. H. Arguello and G. R. Arce, "Code aperture optimization for spectrally agile compressive imaging," J. Opt. Soc. Am. A **28**, 2400–2413 (2011).
8. C. Slinger, H. Bennett, G. Dyer, N. Gordon, D. Huckridge, M. McNie, R. Penney, I. Proudler, K. Rice, K. Ridley, L. Russell, G. de Villiers, and P. Watson, "Adaptive coded-aperture imaging with subpixel superresolution," Opt. Lett. **37**, 854–856 (2012).
9. A. A. Wagadarikar, N. P. Pitsianis, X. Sun, and D. J. Brady, "Video rate spectral imaging using a coded aperture snapshot spectral imager," Opt. Express **17**, 6368–6388 (2009).
10. Y. Wu, C. Chen, Z. Wang, P. Ye, G. R. Arce, D. Prather, and G. J. Schneider, "Fabrication and characterization of a compressive-sampling multispectral imaging system," Opt. Eng. **48**, 123201 (2009).
11. S. K. Nayar, V. Branzoi, and T. E. Boult, "Programmable imaging using a digital micromirror array," in *Proceedings of the IEEE Computer Society Conference on Computer Vision and Pattern Recognition (CVPR 2004)* (2004), Vol. **1**, pp. I–436–I–443.
12. N. Schuster and J. Franks, "Challenges, constraints and results of lens design in 8-12 micron waveband for bolometer-FPAs having a pixel pitch 12 micron," Proc. SPIE **8704**, 870424 (2013).
13. F. de la Barrière, G. Druart, N. Guérineau, J. Taboury, J. Primot, and J. Deschamps, "Modulation transfer function measurement of a multi-channel optical system," Appl. Opt. **49**, 2879–2890 (2010).
14. H. Arguello, C. V. Correa, and G. R. Arce, "Fast lapped block reconstructions in compressive spectral imaging," Appl. Opt. **52**, D32–D45 (2013).
15. M. Figueiredo, R. D. Nowak, and S. J. Wright, "Gradient projection for sparse reconstruction: application to compressed sensing and other inverse problems," IEEE J. Sel. Top. Signal Process. **1**, 586–597 (2007).